

Weak Radio Frequency Signal Detection Based on Piezo-Opto-Electro-Mechanical System: Architecture Design and Sensitivity Prediction

Shanchi Wu, Chen Gong, Chengjie Zuo, Shangbin Li, Junyu Zhang, Zhongbin Dai, Kai Yang, Ming Zhao, Rui Ni, Zhengyuan Xu, and Jinkang Zhu

Abstract—We propose a novel radio-frequency (RF) receiving architecture based on micro-electro-mechanical system (MEMS) and optical coherent detection module. The architecture converts the received electrical signal into mechanical vibration through the piezoelectric effect and adopts an optical detection module to detect the mechanical vibration. We analyze the response function of piezoelectric film to an RF signal, the noise limited sensitivity of the optical detection module and the system transfer function in the frequency domain. Finally, we adopt simple on-off keying (OOK) modulation with bandwidth 1 kHz and carrier frequency 1 GHz, to numerically evaluate the detection sensitivity. The result shows that, considering the main noise sources in wireless channel and circuits, the signal detection sensitivity can reach around -160 dBm with a 50Ω impedance. Such sensitivity significantly outperforms that of the currently deployed Long Term Evolution (LTE) system, when normalizing the transmission bandwidth also to 1 kHz.

Index Terms—weak power signal, radio frequency communication, sensitivity power level, piezo-opto-electro-mechanical system, piezoelectric film, optical coherent detection.

I. INTRODUCTION

HIGH sensitivity signal detection of weak radio frequency (RF) signals is a long and ubiquitous challenge, crucial in radio astronomy, medical imaging, navigation, and communication [1]. Due to rapid development of wireless communications, more compact amplifier, filter, oscillator and mixer circuits are being designed and delivered. Currently, due to wider usage of higher frequency for wireless communication, the faster signal attenuation also requires high-sensitivity signal detection to extend the communication range.

On the other hand, the state-of-the-art signal detection operates using the components based on electro-mechanical interaction. The interaction between optics, electronics and mechanics can further increase the detection sensitivity. The main limit of signal detection sensitivity originates from all types of noise, while the conversion of mechanically mediated

microwave and optical signals can theoretically be close to unit efficiency and zero noise temperature [2]–[8]. Applying such systems to the nano-scale systems (limiting electromagnetic and displacement fields to submicron sizes) provides opportunities for enhancing the coupling strength and increase the receiver sensitivity [9].

From the general theory of electromagnetics, the control of the propagation and conversion of light can be achieved by changing the refractive index in a particular medium, or by changing the physical boundary between different media. The refractive index of materials can be changed in a variety of ways, such as electric field [10] and temperature [9]. The disadvantage of these methods lies in the weak variations. In contrast, the change of mechanical displacement have a significant effect on light control (e.g. the phase of the beam and the frequency of the light in cavity), and the movement of the machinery can be easily driven by electrostatic or piezoelectric force. The study of cavity optical mechanics [11], [12] shows that the nano-mechanical resonators can be strongly coupled with microwaves [13]–[15] or optical fields [16], [17]. Such characteristics increase the possibility for us to convert the RF signal to the optical signal. It is reported that high sensitivity nanometer opto-electro-mechanical system can be achieved by using high quality factor nano-film [1]. Through the coupling inductor, the input microwave signal enters the LC circuit and is loaded on the film. Under the electrostatic force, the film vibrates and the laser phase incident on the surface changes. Consequently, the small film vibration can be detected at the back end. However, electrostatically driven nanoscale opto-electro-mechanical system has a low working frequency range (several Mega Hertz), which cannot meet the Giga Hertz frequency in RF communication systems. Therefore, a piezoelectric actuated opto-electro-mechanical system is desirable for RF frequency up to Giga Hertz. Although piezoelectric micro-electro-mechanical system (MEMS) resonators have been effectively used as frequency determining elements [18]–[20], there is no open report on using the vibration characteristics of piezoelectric MEMS for communication applications.

In this work, we propose an RF receiving system architecture based on the piezoelectric MEMS and optical coherent detection, called piezo-opto-electro-mechanical system (POEMS). To evaluate its feasibility in signal detection, we analyze the response function of piezoelectric film to an RF signal, and obtain the surface vibration equation. Based on the

This work was supported in part by National Key Research and Development Program of China under Grant 2018YFB1801904), Key Program of National Natural Science Foundation of China (Grant No. 61631018), Key Research Program of Frontier Sciences of CAS (Grant No. QYZDY-SSW-JSC003), and Huawei Innovation Project.

Shanchi Wu, Chen Gong, Chengjie Zuo, Shangbin Li, Junyu Zhang, Zhongbin Dai, Kai Yang, Ming Zhao, Zhengyuan Xu, and Jinkang Zhu are with University of Science and Technology of China, Email address: {wsc0807, jy970102, dzbl23, wulikai}@mail.ustc.edu.cn, {cgong821, czuo, shbli, zhaoming, zuzy, jkzhu}@ustc.edu.cn.

Rui Ni is with Huawei Technology, Email address: raney.nirui@huawei.com.

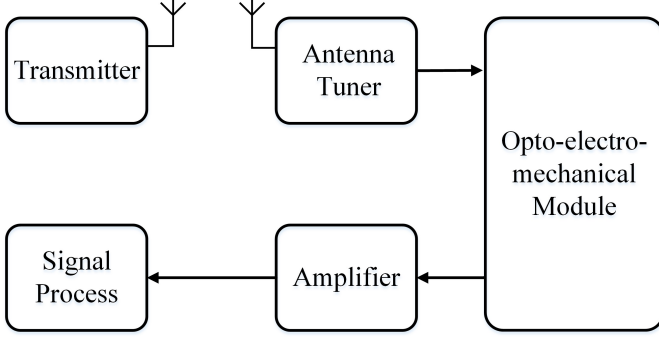


Fig. 1. The diagram of the proposed system.

noise limited sensitivity of the optical detection module, we give the detection sensitivity to different frequencies signals. Furthermore, we characterize the transfer function of POEMS in the frequency domain, based on the first order perturbation theory. Finally, considering noise signals from wireless channel, coupling circuit, piezoelectric film and optical module, we evaluate the performance of an on-off keying (OOK) modulation at bandwidth 1 kHz and carrier frequency 1 GHz. It is calculated that the detection sensitivity can be significantly improved, compared with that of the currently used communication system. Such results envisage the promise of using POEMS for high-sensitivity signal detection.

The remainder of this paper is organized as follows. In Section II, we elaborate the proposed system model under consideration. In Section III, we investigate the response functions of each module and the entire system, and provide the noise characterization and sensitivity limit. Numerical results of each module are given in Section IV. In Section V, we perform link simulation of our proposed system and evaluate the system performance. Finally, Section VI provides the concluding remarks.

II. SYSTEM MODEL

A. System Diagram

We consider a novel piezo-opto-electro-mechanical structure for weak power detection. The input signal is converted to mechanical vibration through the piezoelectric film, and the mechanical vibration is then converted to optical signal through an optical measurement system. The physical size of the piezoelectric film is in the order of submillimeter; and the band pass characteristics of piezoelectric film can realize frequency filtering effect. The diagram of the system under consideration is shown in Figure 1.

We adopt piezoelectric film coated with reflective surface as an "end mirror" of the optical detection module. When the piezoelectric film deforms, the end mirror position changes. The movement of piezoelectric film, which is driven by the RF signal, can be detected by the optical module output. As shown in Figure 2, the RF signal is coupled into the resonant circuit consisting of inductors and piezoelectric film. The film vibrates under the RF signal excitation, and the detected signal of the

photodetector varies accordingly. The piezoelectric film and optical module will be characterized in detail in the subsequent subsections.

B. Piezoelectric Film

Piezoelectric materials have the property that an electric field applied in the direction of polarization can lead to the deform, due to the polarization effect of the dielectric. Aluminium nitride (AlN) is one of them, which has high thermal conductivity at low temperatures, good mechanical strength, high resistivity and corrosion resistance, and high resonant frequency. Thus, AlN resonators are attractive building blocks for electromechanical devices in micrometer and nanometer scales [21]–[23].

The piezoelectric body can generate certain vibration mode activated by the external electric field. If an electric field is applied along a certain direction of the piezoelectric body, the non-zero piezoelectric constant associated with that direction can be employed to determine which vibration mode is likely to be excited. For weak RF signal reception, the thin film system has a linear response to external field strength. Although its three-dimensional system displacement is difficult to characterize, we adopt one directional responses for real applications, which approximately follows Hook law.

As shown in Figure 3 (a), the piezoelectric film adopted exhibits a sandwich structure, with an AlN thin film coated with metal layer as electrodes on the top and bottom surfaces, with length L , width W and thickness L_T . Figure 3 (b) illustrates the shape in cross section, with and without electrical signal. In order to achieve vibration in the thickness direction and ignore the effects of vibration in other directions, the length and width of the film should be much larger than its thickness, i.e., $L, W \gg L_T$. It is important to note that the resonance frequency of the film (vibration in the direction of thickness) under consideration is determined by the thickness. Given piezoelectric material, the resonance frequency f_0 is inversely proportional to thickness. When we apply a signal of certain amplitude with frequency f between two electrodes, the maximum deformation occurs at $f = f_0$.

C. Optical Module

Laser interferometer, as a type of precise optical measuring instrument based on the light interference, can measure the difference of optical paths generated by other certain relevant physical quantities. A typical laser interferometer consists of laser light source, splitting mirror, reflection mirror, polarizing optics and photoelectric detectors. Its basic structure is Michelson interferometer. Any change of optical path difference between two coherent beams will lead to the change of interference field (such as the movement of fringes, etc.), and the optical path change of a coherent beam is caused by the change of geometric path or refractive index of the medium through which it passes. The modern laser interferometer is based on the frequency stabilized laser with high stability of wavelength, whose measurement accuracy is significantly higher than that of other measurement methods. Optical interferometer has been adopted for measurement

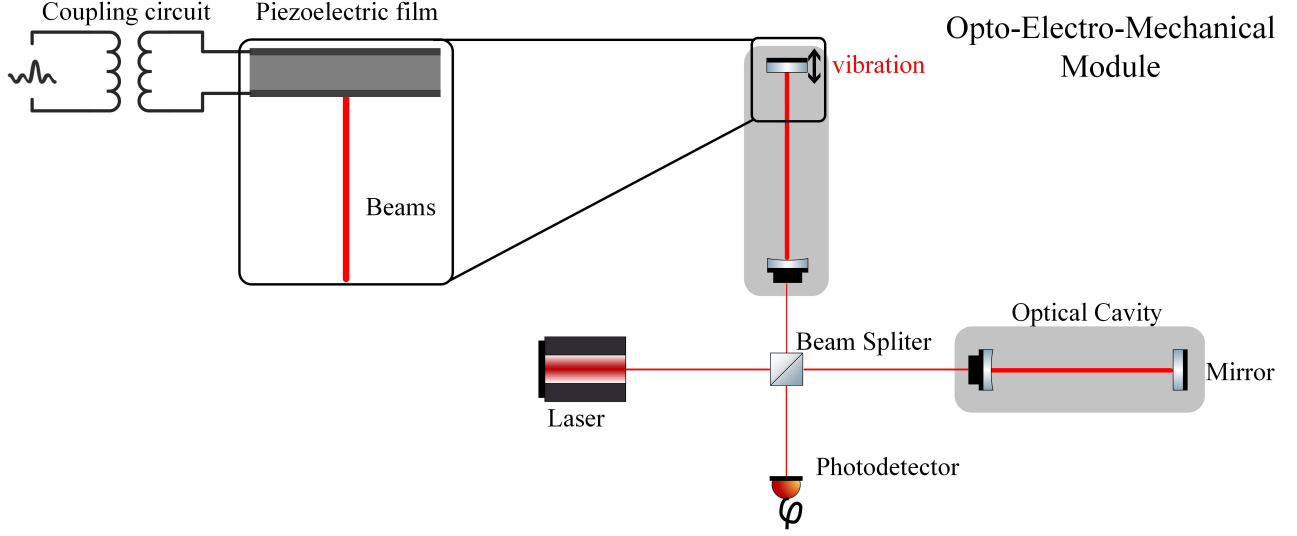


Fig. 2. Diagram of the piezo-opto-electro-mechanical system.

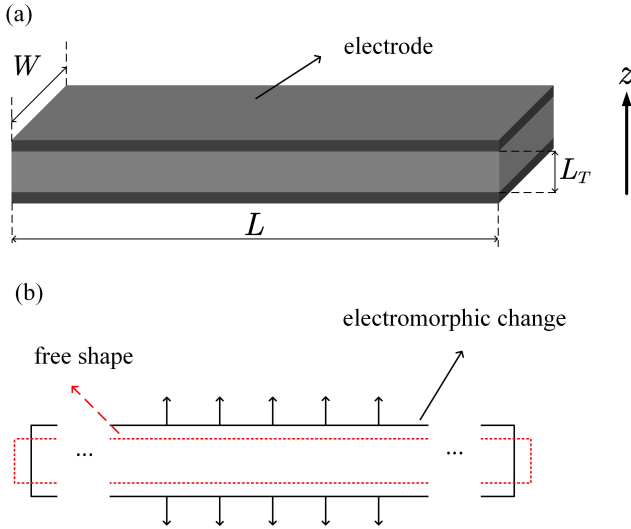


Fig. 3. The sandwich structure of piezoelectric film adopted, with length L , width W and thickness L_T , along with the schematic diagram.

in astronomy, optics, engineering surveying, oceanography, seismology, spectrum analysis, quantum physics experiment, remote sensing and radar. The prototype of Laser Interferometer Gravitational-Wave Observatory (LIGO) system is a Michelson optical interferometer [24].

We design the optical module to realize an optical interferometer, which utilizes the superposition of optical wave to obtain the phase information. As the vibration amplitude of piezoelectric film is tiny under the weak RF signal stimulation, high-precision displacement measurement is required, based on the optical coherent detection following the idea of Michaelson interferometer. When a small shift of the end mirror occurs, the signal strength of the photodetector changes accordingly, caused by the phase change of the light

in optical arm. In order to achieve higher precision, larger laser power and a longer light arm is desirable. In order to decrease the receiver module size, we adopt optical cavity, which significantly increases the measurement precision [25].

III. SENSITIVITY ANALYSIS

We analyze the response of the piezoelectric film and the optical measurement module, based on which the system transfer function in the frequency domain can be obtained. As a major system degradation factor, the noise components from film, circuits and optical module are characterized. Combined with the transfer function, we can obtain the sensitivity of the receiver modules. The analysis will follow the blocks as shown in Figure 4. Firstly, we give the response of piezoelectric film to signals, which converts electrical signal to mechanical displacement. Secondly, the response of optical module to mechanical vibration is investigated, which converts mechanical signal to optical phase. Then, based on the discrete modules, the system transfer function from electrical signal to optical phase is obtained. Finally, considering the noise source, we analyze the noise limited sensitivity.

A. Response of Piezoelectric Film to Signals

The alternating voltage is applied to the piezoelectric vibrator, and the mechanical vibration of the piezoelectric vibrator will be excited by the inverse piezoelectric effect coupling, which will generate strain in the vibrator. Moreover, the mechanical vibration of the vibrator will generate current through the positive piezoelectric effect and feedback back to the circuit. When the applied driving voltage frequency is close to the eigen mechanical resonance frequency of the oscillator, the resonance will lead to large mechanical vibration amplitude. The overlap of the driving current and the feedback current may increase the current flowing through the oscillator. The impedance and admittance frequency characteristics of

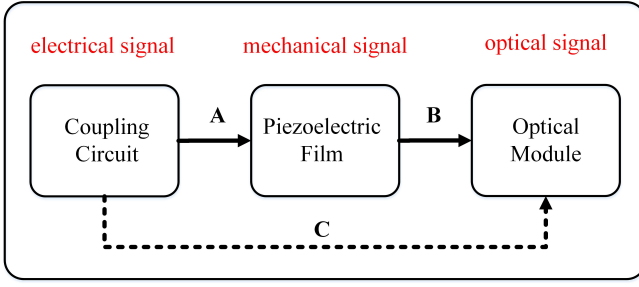


Fig. 4. Diagram of the sensitivity analysis flow.

piezoelectric vibrators close to resonant frequencies can be approximated by an equivalent circuit.

Assume that the film length and width is significantly larger than the thickness, i.e., $L, W \gg L_T$. The thickness direction is the main factor. Thus, only the effect of stress component T_z is considered, and other stress components can be ignored. As the electrode surface is perpendicular to the z axis, only the effect of electric field component E_z is considered, and other electric field components can also be ignored. In addition, because only the edges of the film are fixed, the central part is free, i.e., the boundary condition of two surfaces in z -axis is free. The stress component T_z is equal to zero, and the electrode surface is equipotential. In this case, we can choose T_z and E_z as independent variables and use the first class of piezoelectric equations as follows,

$$\begin{aligned} T_z &= c^E S_z - e_{33} E_z, \\ D_z &= e_{33} S_z + \epsilon^S E_z, \end{aligned} \quad (1)$$

where T_z, S_z, E_z, D_z represent stress field, strain field, electric field and electric displacement vector components along the z -axis, respectively; c^E is the elastic modulus at constant electric field strength and ϵ^S is the relative permittivity at constant strain field strength; and e_{33} is piezoelectric constant decided by material [26]. Typically, c^E and ϵ^S are treated as constants. Here, all vector variables are expressed as scalars since we only consider one-dimensional vibration. For convenience, in the following derivations, the letter subscript indicating the z direction is neglected, shown as follows,

$$\begin{aligned} T &= c^E S - e_{33} E, \\ D &= e_{33} S + \epsilon^S E. \end{aligned} \quad (2)$$

Letting u represent the displacement in z -axis, given that the displacement of the piezoelectric film is treated as an elastic harmonic oscillator, we have

$$\begin{aligned} \frac{\partial^2 u}{\partial t^2} &= \frac{c^D}{\rho} \frac{\partial^2 u}{\partial z^2}, \\ c^D &= c^E + \frac{e_{33}^2}{\epsilon^S}, \end{aligned} \quad (3)$$

where ρ is the mass density of the film and c^D is the elastic modulus at constant electric displacement vector [27].

Considering the separation of variables, i.e., $u(z, t) = Z(z) \cdot e^{j\omega t}$, and defining phase velocity $c_v \triangleq \sqrt{\frac{c^D}{\rho}}$ of the vibration

module along the z -axis, the wave equation $Z(z)$ is given as follows,

$$\begin{aligned} \omega^2 Z + \frac{c^D}{\rho} \frac{d^2 Z}{dz^2} &= 0, \\ \frac{d^2 Z}{dz^2} + \frac{\omega^2}{c_v^2} Z &= 0. \end{aligned} \quad (4)$$

We give one solution to the above equation.

Theorem 1 Under excitation signal $V = V_0 \cdot e^{j\omega_r t}$ and free boundary condition $T_{z=0} = T_{z=L_T} = 0$, the surface vibration at $z = L_T$ is given by

$$u(L_T, t) = \frac{e_{33} D_0}{\epsilon^S c^D \beta} \tan\left(\frac{\beta L_T}{2}\right) \cdot e^{j\omega_r t}, \quad (5)$$

where D_0 is the amplitude of electric displacements vector; $\beta \triangleq \frac{\omega_r}{c_v}$ is a defined coefficient; and ω_r is the resonant frequency.

Proof: Please refer to Appendix B-A. ■

In a real system, the relationship between force and strain may not be linear. Accordingly, parameters such as damping coefficient η is introduced to characterize the new system, which can be written as $T = c^D S + \eta \frac{dS}{dt}$.

Letting u represent the displacement in the z -axis, under the condition that the displacement of the piezoelectric film is treated as a damped elastic harmonic oscillator, the wave equation satisfied by the displacement in damping system is given by

$$c^D \frac{\partial^2 v}{\partial z^2} + \eta \frac{\partial^3 v}{\partial t \partial z^2} = \rho \frac{\partial^2 v}{\partial t^2}, \quad (6)$$

where $v(z, t) = \frac{\partial u(z, t)}{\partial t}$ represents the vibration velocity; ρ represents the mass density of the film; and c^D is the elastic modulus at constant electric displacement vector [27].

We give one solution to the above equation.

Theorem 2 For piezoelectric film system with damping coefficient η , under the excitation signal $V = V_0 \cdot e^{j\omega_r t}$ and boundary condition $T_{z=0} = T_{z=L_T} = 0$, the surface vibration at $z = L_T$ is given by

$$u(L_T, t) \approx -j \frac{4V_0 d_{33} Q}{\pi^2} \cdot e^{j\omega_r t}, \quad (7)$$

where d_{33} is the Piezoelectric constant and $Q = \left(\frac{\eta \omega_r}{c^D}\right)^{-1}$ is the quality factor; and ω_r is the resonant frequency.

Proof: Please refer to Appendix B-B. ■

B. Response of Optical Module to Piezoelectric Film Vibration

For classical Michelson interferometer, the beam propagation can be represented by electric field, as shown in Figure 5 [25]. Assuming that all parameters of the optical components are known, the output of optical field is characterized as follows,

$$\begin{aligned} E_5 &= E_0 \left(Re^{i(2\varphi_{r1} + \Phi_1)} + T e^{i(2\varphi_t + \Phi_2)} \right), \\ E_6 &= E_0 r t \left(e^{i(\varphi_t + \varphi_{r1} + \Phi_1)} + e^{i(\varphi_t + \varphi_{r2} + \Phi_2)} \right), \end{aligned} \quad (8)$$

where $\varphi_{r1}, \varphi_{r2}$ and φ_t are phase differences caused by reflection of upper surface, lower surface and transmission

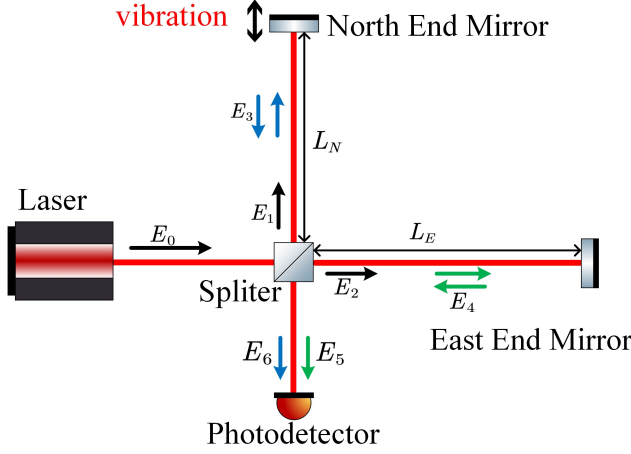


Fig. 5. Diagram of Michaelson interferometer.

of the mirror, respectively; r and t are the reflectivity and transmittivity of end mirrors, respectively; Φ_1 and Φ_2 are phase differences caused by optical path differences in arms, respectively; and $R = r^2$ and $T = t^2$.

In a real systems, we can only perform direct detection on the optical power or intensity. It is difficult to obtain the optical signal frequency of the commonly used laser directly through the photoelectric sensor. A common solution is to detect the beat of the coherent signal, which is the envelope of the intensity of two overlapping and coherent fields. For the output light field with two frequency components $E = E_0 [\cos(\omega_1 t) + \cos(\omega_2 t)]$, the corresponding output power is

$$P = E_0^2 \left(\cos^2(\omega_1 t) + \cos^2(\omega_2 t) + \cos(\omega_+ t) + \cos(\omega_- t) \right), \quad (9)$$

where $\omega_+ = \omega_1 + \omega_2$ and $\omega_- = \omega_1 - \omega_2$. We can filter out the high frequency component and recover the signal.

For any interferometer systems, the optical arm length variation will affect the laser propagation in space and cause the phase variation. In order to analyze the influence of the moving end mirror frequency on the output sideband signal, we apply periodic modulation signal $h(t) = h_0 \cos(\omega_x t + \varphi_x)$ to the optical arm, as shown in Figure 5. We have the following results on the output signal of the light field. The output signal of the light field after the reflection signals from the N-end mirror and E-end mirror, combined by the beam splitting mirror, is given by

$$\begin{aligned} E_{\text{out}} &= iE_0 \cos(k_0 \Delta L) + b_N^+ + b_N^- + b_E^+ + b_E^- \\ &= iE_0 \frac{w_0 h_0}{\omega_x} \sin(k_x \bar{L}) \sin(k_0 \Delta L) \cos(\omega_x t - k_x \bar{L} + \varphi_x) + \\ &\quad iE_0 \cos(k_0 \Delta L), \end{aligned} \quad (10)$$

where E_0 , k_0 and ΔL are the amplitude, wave vector and optical arm length differences of the carrier field, respectively; b_N^\pm and b_E^\pm are signal sidebands in two optical arms [25].

The light signal power can be expressed as the power of the electric component, and the output signal power is propotional

to the following,

$$P_x = |E_0|^2 \frac{w_0 h_0}{\omega_x} \sin(k_x \bar{L}) \sin(2k_0 \Delta L) \cos(\omega_x t - k_x \bar{L} + \varphi_x), \quad (11)$$

where $\bar{L} = \frac{L_N + L_E}{2}$ is the average optical arms length.

C. Transfer Function of Opto-Electro-Mecahnical System in the Frequency Domain

In general, the internal energy of a piezomechanical system is given by

$$U_{pe} = \frac{1}{2} \int dv (\mathbf{T} \cdot \mathbf{d}^T \cdot \mathbf{E} + \mathbf{E} \cdot \mathbf{d} \cdot \mathbf{T}), \quad (12)$$

where \mathbf{T} and \mathbf{S} are the stress and strain fields, respectively; and \mathbf{E} and \mathbf{D} are the electric and electric displacement fields, respectively [28].

For one-dimension condition, we only consider the components along z-axis. The total energy of piezoelectric oscillator is given by

$$\begin{aligned} U &= \frac{1}{2} \int dv [T_z \cdot (s_{33} T_z + d_{33} E_z) + E_z \cdot (d_{33} T_z + \epsilon_{33} E_z)] \\ &= \frac{1}{2} \int dv (s_{33} T_z^2) + \frac{1}{2} \int dv (\epsilon_{33} E_z^2) + \\ &\quad \frac{1}{2} \int dv (T_z \cdot d_{33} E_z + E_z \cdot d_{33} T_z) \\ &\triangleq U_p + U_e + U_{pe}, \end{aligned} \quad (13)$$

where U_p , U_e and U_{pe} represent mechanical energy, electrical energy and electromechanical coupling energy, respectively. According to the three parts of energy, the Hamiltonian form is given by,

$$\begin{aligned} H &= \frac{p^2}{2m} + \frac{m\omega_M^2 x^2}{2} + \frac{\phi^2}{2L_0} + \frac{q^2}{2C(x)} + \\ &\quad 2g \sqrt{\frac{m\omega_M}{C(x)\omega_{LC}}} xq - qV, \end{aligned} \quad (14)$$

where x and p are the displacement and momentum, respectively; q and ϕ are the charge and flux, respectively. We have the following results on the transfer function of the proposed piezo-opto-electro-mechanical system.

Theorem 3 Assuming that δF_{th} , $\delta \varphi_{im}$ and δV are random thermal disturbance dynamics, optical phase uncertainty and electric signal, respectively, the transfer function of the proposed piezo-opto-electro-mechanical system in the frequency domain is given by

$$\begin{aligned} \delta x(\omega) &= \chi_m^{eff} (-\delta F_{th}(\omega) + G \chi_{LC}(\omega) \delta V(\omega)), \\ \delta \varphi(\omega) &= 2k \chi_m^{eff} (-\delta F_{th}(\omega) + G \chi_{LC}(\omega) \delta V(\omega)) \\ &\quad + \delta \varphi_{im}(\omega), \\ \chi_m(\omega) &\triangleq \frac{1}{m(\omega_m^2 - \omega^2 - i\omega\Gamma_m)}, \\ \chi_{LC}(\omega) &\triangleq \frac{1}{L_{LC}(\omega_{LC}^2 - \omega^2 - i\omega\Gamma_{LC})}, \\ \chi_m^{eff}(\omega) &\triangleq (\chi_m(\omega)^{-1} - G^2 \chi_{LC}(\omega))^{-1}, \end{aligned} \quad (15)$$

where m and L_{LC} are equivalent mass of piezoelectric oscillator and inductance in the resonant circuit, respectively; ω_m and ω_{LC} are resonance frequencies of oscillator and LC circuit, respectively; Γ_m and Γ_{LC} are the damping coefficients of the piezoelectric film and the LC resonant circuit, respectively; and G is the coupling coefficient.

Proof: Please refer to Appendix B-C. ■

The output signal in the system transfer function can be represented by the optical phase signal. With respect to the signal power spectral density, the transfer function is obtained as follows,

$$S_{\varphi\varphi}^{output} = (2k)^2 |\chi_m^{eff}|^2 (|G\chi_{LC}|^2 S_{VV}^{electro} + S_{FF}^{th}) + S_{\varphi\varphi}^{imp}, \quad (16)$$

where $S_{VV}^{electro}$, S_{FF}^{th} and $S_{\varphi\varphi}^{imp}$ are signal power spectral densities of the input, the force on film and the optical phase, respectively [1].

D. Noise Characterization

The main noise sources are from circuits, thermal environment and optical module. Firstly, we analyze the electrical noise of the wireless channel, antenna, resonant circuit and the dynamic displacement disturbance of film. Secondly, when the classical noise in the system is small enough, the influence of quantum fluctuation noise of the optical module becomes critical. Here we consider two types of noise sources: optical radiation pressure and quantum fluctuation of light. Finally, combined with the transfer function, we can obtain the equivalent input noise in electrical domain.

1) *Electrical Input Noise:* Assuming that the wireless channel introduces additive white Gaussian noise, we adopt an equivalent resistance thermal noise to characterize it. Antenna noise sources include thermal noise, solar radiation, cosmic radiation, electromagnetic radiation and electromagnetic leakage. Other types of noise are considered to be cancelable under certain conditions, except for thermal noise. For LC resonant circuit, inductor thermal noise, shot noise and pink noise are three main types of noises. At low frequencies, the pink noise is several times larger than the shot noise, but our system works in a high frequency and can effectively reduce the influence of pink noise. Besides, since the shot noise is weaker than thermal noise under consideration, we only consider thermal noise. Additional noise due to nonstationary radio frequency interference from cellular phones, vehicles, etc., needs to be considered, but in this analysis we will concentrate on natural sources only. The total input noise power spectral density can be given by

$$N_{VV}^{electro}(\omega) = k_B R_{50\Omega} (T_{ant} + G_A T_{bg} + T_{LC}), \quad (17)$$

where T_{bg} , T_{ant} and T_{LC} are equivalent noise temperature of wireless channel, antenna and resonant circuit, respectively; $R_{50\Omega}$ is a 50Ω impedance matching resistance; k_B is the Boltzmann constant and G_A is the gain of antenna.

2) *Film Thermal Noise:* In the LC resonant circuit, the piezoelectric film acts as a capacitor, whose noise is considered in film thermal noise. Such noise is not white in the frequency domain, while the disturbing force from environment

is a Gaussian white noise instead. We called this dynamic displacement disturbance of film as its thermal noise, which is driven by a disturbing force from environment.

Theorem 4 *In equilibrium, the environment exerts a disturbing force η on the damped harmonic oscillator. According to the white noise hypothesis, $\eta(t)$ satisfy $\langle \eta(t) \rangle = 0$ and $\langle \eta(t)\eta(\tau) \rangle = 2\alpha\delta(t-\tau)$. The equivalent harmonic noise power spectrum of the piezoelectric film is given by*

$$N_{xx}^{film}(\omega) = 2\alpha_{ex} |\chi_m(\omega)|^2, \quad (18)$$

where $\alpha_{ex} = \alpha m_{eff}^2$ represents the strength of noise.

Proof: Please refer to Appendix B-D. ■

3) *Optical Module Noise:* In the optical cavity, the noise power spectral densities of the quantum noise and optical radiation pressure noise are given by

$$N_{xx}^{imp}(\omega) = \frac{\kappa}{16\bar{n}_{cav}G^2} \left(1 + 4\frac{\omega^2}{\kappa^2}\right), \quad (19)$$

and

$$N_{xx}^{FF}(\omega) = \bar{n}_{cav} \frac{4\hbar^2 G^2}{\kappa} \left(1 + 4\frac{\omega^2}{\kappa^2}\right)^{-1} |\chi_m(\omega)|^2, \quad (20)$$

respectively, where κ and G are cavity decay and coupling coefficient, respectively; and \bar{n}_{cav} is the average number of photons in cavity [12].

The optical module noise under consideration can be given by

$$\begin{aligned} N_{xx}^{optical}(\omega) &= N_{xx}^{imp}(\omega) + N_{FF}(\omega) |\chi_m(\omega)|^2 \\ &= \frac{C}{16\bar{n}_{cav}} + \frac{4\hbar^2 \bar{n}_{cav}}{C} |\chi_m(\omega)|^2 \\ &\geq 2\sqrt{\frac{C}{16\bar{n}_{cav}} \cdot \frac{4\hbar^2 \bar{n}_{cav}}{C}} |\chi_m(\omega)|^2 \\ &= \hbar |\chi_m(\omega)|, \end{aligned} \quad (21)$$

where $C \triangleq \kappa \left(1 + 4\frac{\omega^2}{\kappa^2}\right) / G^2$ is a defined coefficient. It should be noted that the noise of optical module is typically represented by the phase uncertainty. Since the optical module is employed to measure the film vibration, we convert the displacement noise into the phase noise as follows,

$$N_{\varphi\varphi}(\omega) = k^2 N_{xx}(\omega). \quad (22)$$

4) *Output Noise:* Considering the main noise components in the system, the output noise power spectral density at resonance frequency ω_r is given by

$$N_{\varphi\varphi}^{output} = (2k)^2 \left(N_{VV}^{electro} |\chi_m^{eff} G \chi_{LC}|^2 + N_{xx}^{film} \right) + N_{\varphi\varphi}^{optical}, \quad (23)$$

where χ_{LC} , χ_m^{eff} and G are introduced in Theorem 3.

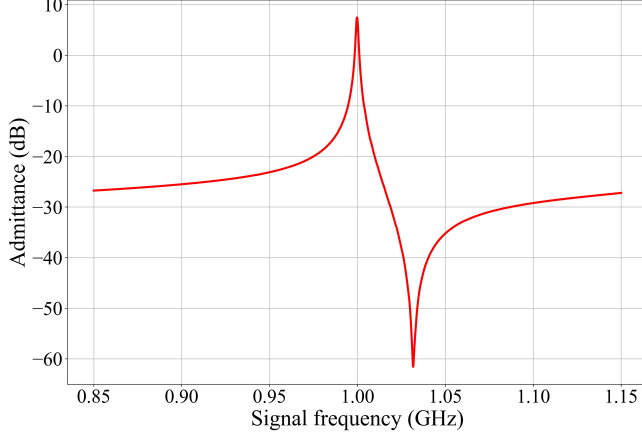


Fig. 6. The simulation of piezoelectric film admittance curves.

E. Sensitivity Limit

According to Eq.16 and Eq.23, the system output signal to noise ratio can be given by

$$SNR = \frac{(2k)^2 S_{VV}^{electro} \left| \chi_m^{eff} G_{\chi LC} \right|^2}{(2k)^2 \left(N_{VV}^{electro} \left| \chi_m^{eff} G_{\chi LC} \right|^2 + N_{xx}^{film} \right) + N_{\varphi\varphi}^{optical}}. \quad (24)$$

The minimum signal power spectral density for $SNR = 0dB$ is given by

$$S_{VV}^{min} = \underset{S_{VV}}{Arg} \{ SNR = 0dB \}. \quad (25)$$

Assuming that the signal bandwidth is B , the minimum signal power is given by

$$P_{min} = S_{VV}^{min} BR_{50\Omega}. \quad (26)$$

IV. NUMERICAL RESULTS ON THE COMPONENTS

A. Piezoelectric Film

COMSOL Multiphysics® is a large-scale advanced numerical simulation software. To simulate all kinds of physical processes, COMSOL Multiphysics® is adopted to realizes highly accurate numerical simulation with high-efficiency computing performance and outstanding multi field bidirectional direct coupling analysis ability. In order to verify the rationality of sensitivity analysis, the admittance curve of the model was simulated and verified by COMSOL Multiphysics® software [29]. We adopt an AlN film that is 5000 microns long, 100 microns wide and 5.85 microns high. The sweep frequency range is set to be 0.85 GHz to 1.15 GHz to include the film resonance frequency. In order to save the running time of the program, the peak response location can be estimated through the theoretical calculation to guide the setting of the sweep frequency range. Finally, the admittance curves is shown in Figure 6. The peak response occurs at the position where frequency approximately equals 1 GHz.

Under the same conditions, we set the excitation signal frequency to be resonance frequency, where the maximum

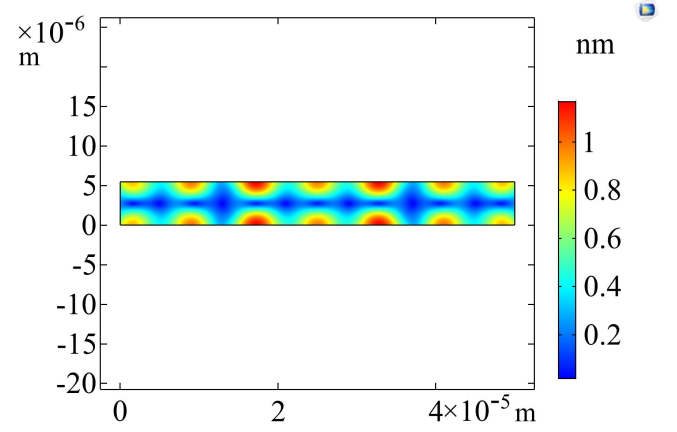


Fig. 7. A regional 2D vibration schematic of piezoelectric film under the RF signal excitation.

admittance is obtained. Assuming that the amplitude of sinusoidal signal is 1 V with zero offset, the film variation along z-axis is shown in Figure 7. Compared with the vibration equations in Section III-A, the theoretical calculation results can well match the simulation results. The relevant parameters in simulation can be seen in Table I. According to Eq. 7, the theoretical amplitude of surface displacement is about 2 nm. The maximum amplitude shown in Figure 7 is about 1.2 nm, matching the theoretical value within 3dB with the same order of magnitude. The possible reason is that the signal frequency does not match the resonant frequency well.

TABLE I
TYPICAL PARAMETERS USED IN COMSOL SIMULATION

Name	Symbol	Value
piezoelectric constant	d_{33}	$4.98 \times 10^{-12} C/N$
piezoelectric constant	e_{33}	$1.55 C/m^2$
piezoelectric constant	s_{33}	d_{33}/e_{33}
modulus of elasticity	c^D	$3 \times 10^{11} N/m^2$
relative permittivity	ϵ_{33}	9
permittivity	ϵ_0	$8.85 \times 10^{-12} F/m$
density of film	ρ	$3230 kg/m^3$
piezoelectric film thickness	L_T	5.85 um
piezoelectric film width	W	100 um
piezoelectric film length	L	5000 um
quality factor of film	Q	1000
resonant frequency of circuit	f_{LC}	1 GHz
resonant frequency of film	f_m	1 GHz

B. Optical Detection Module

Frequency domain Interferometer Simulation Software (FINESSE) is a simulation program for interferometers. For a given optical setup, it computes the light field amplitudes at every point in the interferometer assuming a steady state. The interferometer description is translated into a set of linear equations that are solved numerically, where extensive

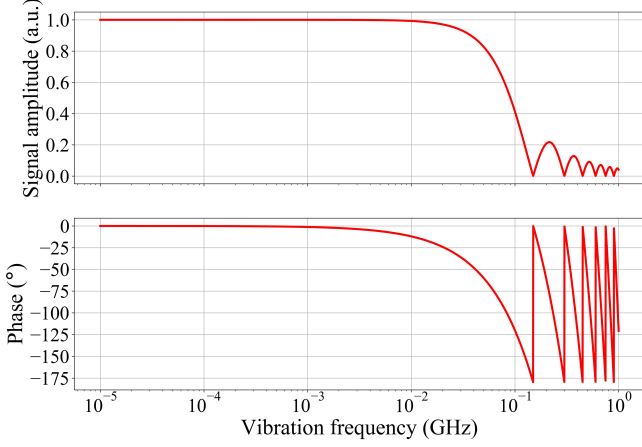


Fig. 8. The response to mirror vibration.

analysis on the performance prediction be performed, including computing the modulation-demodulation error signals and transfer functions. It can also perform the analysis using plane waves or Hermite-Gauss modes, while the latter one allows computing the effects of mode matching and misalignments. In addition, the error signals for automatic alignment systems can be simulated [30]. We use FINESSE to perform simulation. The parameter settings in simulation are achievable in a real system. The simulation includes two parts: response to mirror vibration signal and noise limited sensitivity of optical module. Detailed parameters can be seen in Table II.

1) *Response to Mirror Vibration:* This is a simple FINESSE simulation showing how the response signal can be modulated by the vibration signal on the end mirror. It outputs the amplitude and phase of the upper sideband that reaches the output port. The dips in amplitude occur when the travel time of the photons along the interferometer arms equals one vibration period, and hence the signal accumulated in the first and second half of the travel time cancel each other (the plot above does not have enough resolution to show that the dips indicate zero signal, the non-zero amplitudes are an artefact of the numerical plotting routine) [25]. In the simulation, the frequencies varies from 10 kHz to 1 GHz, as shown in Figure 8. In the low frequency part (≤ 10 MHz), the amplitude of the response signal almost remains unchanged, while the amplitude of the response signal begins to oscillate and decline significantly at high frequencies. As a guide, we design the optical module to create the peak response at the expected frequency 1 GHz.

2) *Noise Limit Sensitivity of Optical Module:* Shot noise is a type of readout noise in experimental observation. When the number of energy-carrying particles (such as electrons in a circuit or photons in an optical instrument) in the observation is small enough to cause observable statistical fluctuations in data reading, the statistical readout fluctuations are called shot noise. Uncertainty of quantum noise and optical radiation pressure noise is described in Section III-D3. It is reported that the noise limited sensitivity at low frequencies (a few tens of Hertz) can reach up to $10^{-23} \text{ m}/\sqrt{\text{Hz}}$, which size

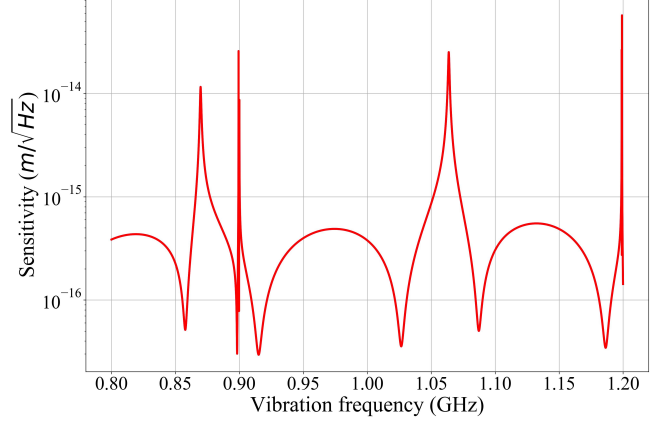


Fig. 9. The noise limited sensitivity.

is several kilometers [25]. This simulation shows the noise limited sensitivity of the proposed optical module at higher frequencies and smaller size. As shown in Figure 9, the detection sensitivity of the optical module fluctuates with frequencies. We can obtain about $5 \times 10^{-17} \text{ m}/\sqrt{\text{Hz}}$ at best.

TABLE II
PARAMETERS USED IN FINESSE SIMULATION

Parameter	Value
east end mirror transmissivity	5×10^{-6}
east end mirror loss	3.75×10^{-5}
east incident mirror transmissivity	0.014
east incident mirror loss	3.75×10^{-5}
north end mirror transmissivity	5×10^{-6}
north end mirror loss	3.75×10^{-5}
north incident mirror transmissivity	0.014
north incident mirror loss	3.75×10^{-5}
beam splitter mirror transmissivity	0.5
beam splitter mirror reflectivity	0.5
north arm length	1 m
east arm length	1 m
laser power	1 W
wavelength	1064 nm
detection sensitivity	$5 \times 10^{-17} \text{ m}/\sqrt{\text{Hz}}$

V. SYSTEM PERFORMANCE EVALUATION

A. Gain from Low Noise Amplifier

We evaluate the link performance via employing a low noise amplifier (LNA) in the system. Assume that the input signal power spectral density is s_I . The next level has certain noise n_{xx} . In our proposed system, n_I and n_{xx} represent noise component in antenna output signal and noise in the piezo-opto-electro-mechanical system, respectively. The system SNR without LNA is given by

$$\text{SNR}_f = \frac{s_I}{n_I + n_{xx}}. \quad (27)$$

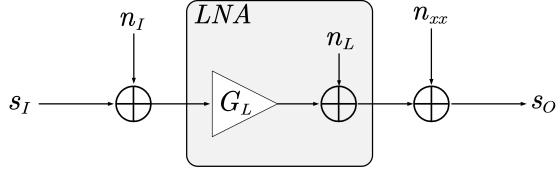


Fig. 10. The signal flow graph of the receiver system with an LNA.

Then, we introduce an LNA with noise n_L and gain $G_L > 1$, as shown in Figure 10. The system SNR at the LNA output can be given by

$$SNR_f^L = \frac{G_L s_I}{G_L n_I + n_L + n_{xx}}. \quad (28)$$

The SNR gain from LNA is given as follows

$$SNR_f^L - SNR_f = \frac{s_I [(G_L - 1) n_{xx} - n_L]}{(G_L n_I + n_L + n_{xx})(n_I + n_{xx})}. \quad (29)$$

When $G_L > G_L^* = n_L/n_{xx} + 1$, the LNA will improve the SNR of the system.

B. System Sensitivity

The system link simulation diagram is shown in Figure 11. The OOK modulation signal is mixed with white Gaussian noise in wireless channel. Then, the antenna receives signal and transmits it to LNA and LC resonant circuit. Finally, the RF signal excites the piezoelectric film to vibrate, leading the variation of light phase in the optical module, which detects the OOK symbols from the output signal. Detailed parameters used in the simulation is shown in Table III.

TABLE III
TYPICAL PARAMETERS USED IN SYSTEM LINK SIMULATION

Name	Symbol	Value
environment temperature	T	300 K
carrier frequency	f_c	1 GHz
signal bandwidth	BW	1 kHz
modulation method	MM	OOK
antenna gain	G_a	15 dB
antenna noise temperature	T_{ant}	100 K
LNA gain	G_L	30 dB
LNA noise temperature	T_{LNA}	25 K
wireless channel noise power	n_w	$5 \times 10^{-21} \text{V}^2/\text{Hz}$
LC circuit noise PSD	n_{LC}	$2.1 \times 10^{-19} \text{V}^2/\text{Hz}$
film noise PSD	n_f	$2.5 \times 10^{-33} \text{m}^2/\text{Hz}$
Note: PSD represents power spectral density, whose units for electric and displacement signals are V^2/Hz and m^2/Hz , respectively.		

For the OOK modulation, the carrier frequency is set to 1 GHz and the bandwidth is set to 1 kHz. Assume that wireless channel noise is white Gaussian noise. We set the antenna gain to be a typical value $G_a = 15$ dB, and adopt the noise temperature model to estimate the noise power spectral density introduced by the antenna to be $n_a = k_B T_{ant} R_{50\Omega} = 6.9 \times 10^{-20} \text{V}^2/\text{Hz}$. The antenna output signal is amplified by

a low noise amplifier with gain $G_L = 30$ dB and noise power spectral density $n_L = k_B T_{LNA} R_{50\Omega} = 1.73 \times 10^{-20} \text{V}^2/\text{Hz}$ [31]. The electrical signal excites the piezoelectric film to vibrate through a coupling circuit, where the response signal is characterized in Section III-C. This process also introduces equivalent film thermal noise in Section III-D2, whose noise power spectral density is $n_f = 2.5 \times 10^{-33} \text{m}^2/\text{Hz}$. Then, the total noise power spectral density as follows,

$$n_{tot} = |\chi_m^{eff}| (G_L (G_a n_w + n_a) + n_L + n_{LC}) + n_f. \quad (30)$$

For signal power -160 dBm, the output signal and several main noise signals is shown in Figure 12. It can be seen that the signal can be differentiated from the noise.

According to the theoretical analysis in Section III, the system sensitivity critically depends on the environment temperature, carrier frequency and channel bandwidth. Figure 13 shows the system sensitivity variation with temperature, carrier frequency and channel bandwidth. The red, green and blue curves are obtained at temperature 300 K, 30 K and 3 K, respectively. The system sensitivity at carrier frequency 1 GHz, 3 GHz and 5 GHz are shown with different markers. We can find that lower temperature and narrower bandwidth lead to higher sensitivity, but the sensitivity is not sensitive to the carrier frequency.

In Appendix A, we calculate the reference sensitivity power levels of evolved universal terrestrial radio access (E-UTRA) base station and narrowband internet of thing (NB-IoT) base station in 4G LTE system. At normalized bandwidth 1 kHz, the highest sensitivities for E-UTRA and NB-IoT base stations are -133.7 dBm and -134.3 dBm, respectively. It shows that about 26 dB gain can be predicted by this prototype design.

C. Signal to Noise Ratio, Bit Error Rate and Capacity

Figure 14 shows the system output SNR with external wireless channel noise power. When the signal power is -160 dBm, for wireless channel noise power -170 dBm, more than 5 dB SNR can be achieved.

We refer to IM/DD Gaussian channel capacity under vector modulation, to evaluate the achievable rate of the proposed piezo-opto-electro-mechanical system [32]. Assuming wireless channel noise power is -160 dBm and dimming coefficient $\xi = 0.5$, we get the upper and lower bounds on the channel capacity results under different received power, as shown in Figure 15.

Under different input power and wireless channel noise power, we perform the bit error rate simulation of the 1 kbps OOK signal, as shown in Figure 16. We can get that the BER is lower than 10^{-4} when the received power is -150 dBm and the wireless channel power is lower than -160 dBm.

VI. CONCLUSION

We have proposed a high sensitivity piezo-opto-electro-mechanical receiver system, which utilizes optical module to detect the piezoelectric film vibration driven by RF signal. Based on the analysis of piezoelectric vibration and optical response to the vibration, we have analyzed the system transfer function in the frequency domain. Both theoretical results and numerical/simulation results are provided to test

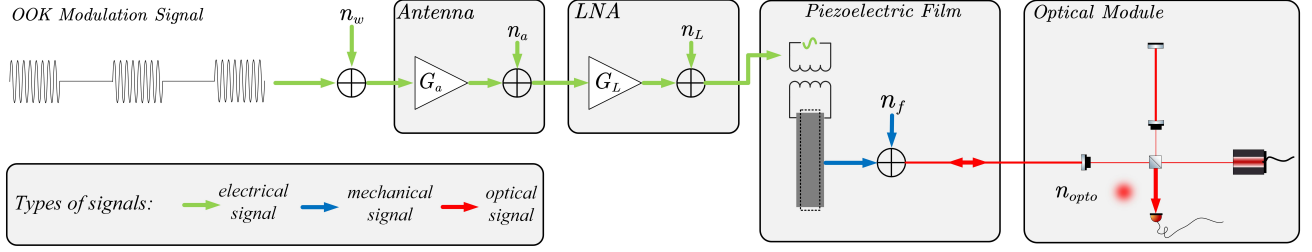


Fig. 11. The signal flow graph in the system link simulation.

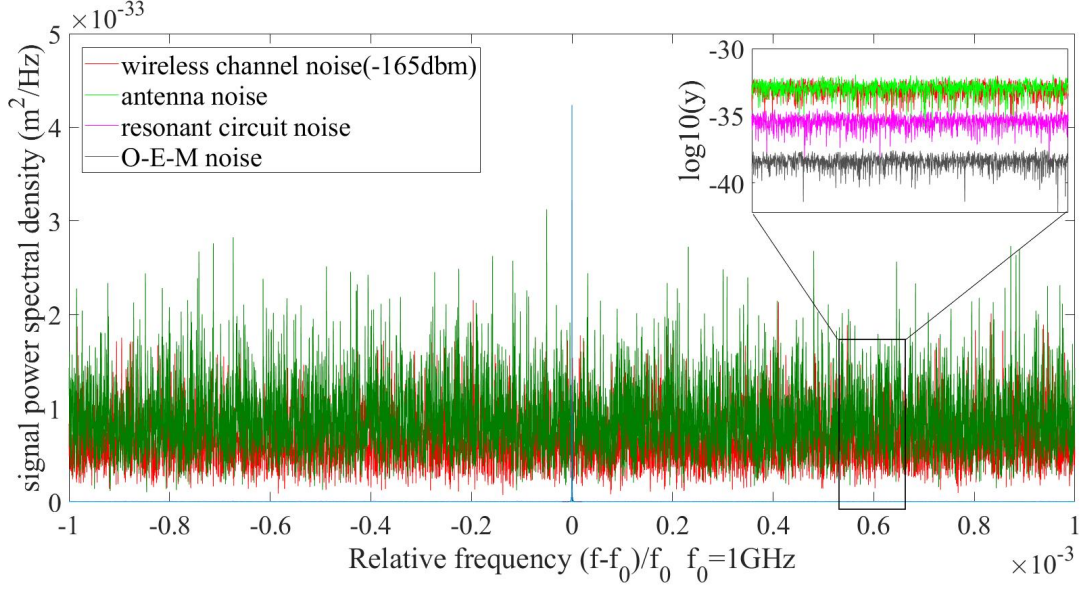


Fig. 12. Signal and noises power spectral densities with input power -160 dBm.

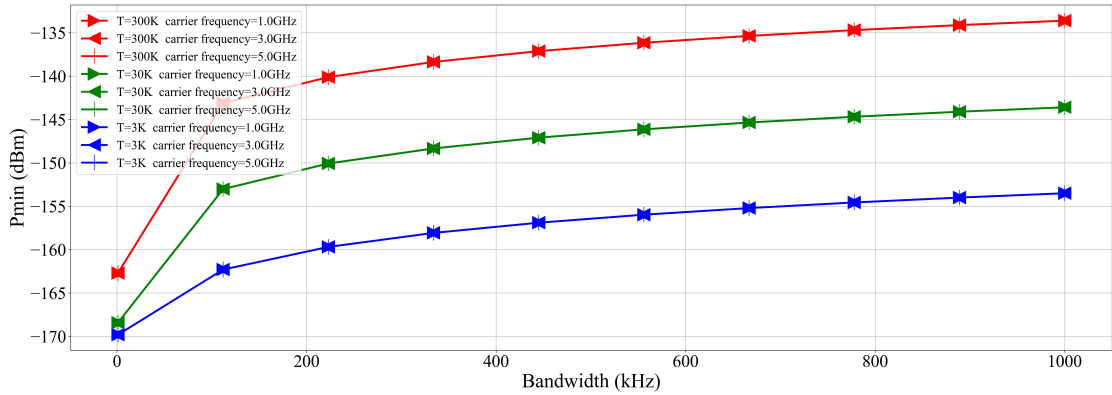


Fig. 13. The influence of temperature, bandwidth and carrier frequency to the system sensitivity. The bandwidth varies from 1 kHz to 1 MHz.

the feasibility of the proposed system. For OOK modulation signal with 1 kHz bandwidth and 1 GHz carrier frequency, the system receiving sensitivity can be predicted to -160 dBm, which significantly outperforms that of the reference sensitivity power of the evolved universal terrestrial radio

access base stations. Future works include the fabrication of the proposed architecture, and the test in various laboratory and practical scenarios.

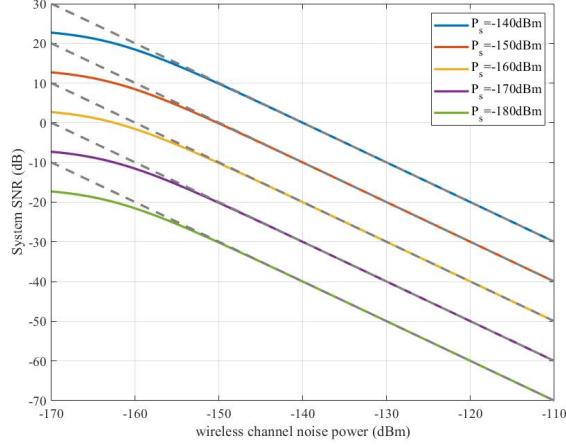


Fig. 14. The SNR of the output signal from optical detection module under different wireless channel noise power.

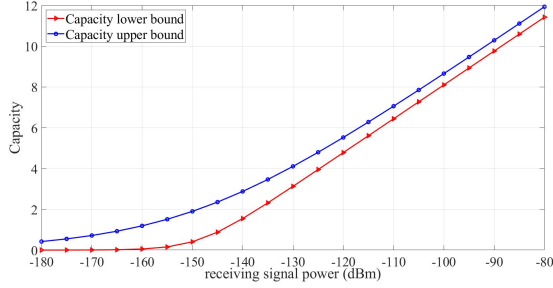


Fig. 15. Upper and lower bounds on the capacity of the system under consideration.

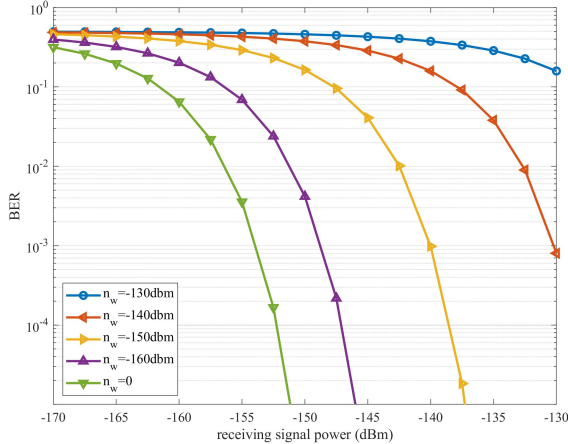


Fig. 16. Bit error rate under different wireless channel noise power level.

APPENDIX A

REFERENCE SENSITIVITY POWER LEVEL

The reference sensitivity power level $P_{REFSENS}$ is the minimum mean power received at the antenna connector at which a throughput requirement shall be met for a specified reference

measurement channel. For evolved universal terrestrial radio access (E-UTRA), the throughput shall be larger than or equal to 95% of the maximum throughput of the reference measurement channel. The reference sensitivity power levels for Wide Area Base Station (BS), Local Area BS, Home BS and Medium Range BS are shown in Table IV [33].

For narrowband internet of thing (NB-IoT) standalone BS or E-UTRA BS with NB-IoT (in-band and/or guard band), NB-IoT throughput shall be larger than or equal to 95% of the maximum throughput of the reference measurement channel. The reference sensitivity power levels for Wide Area BS, Local Area BS, Home BS and Medium Range BS are shown in Table V [33].

Consider encoding rate 1/3 and the decoding is correct around 0 dB. The reference sensitivity at normalized channel bandwidth $B_{NORM} = 1$ kHz is given by

$$P_{NORMSENS} = P_{REFSENS} - 10\log(B_{NORM}/B_{REF}) - 10\log\left(\frac{1}{3}\right), \quad (31)$$

where B_{REF} is the reference bandwidth in Table IV and V. Based on this, the normalized reference sensitivity power levels for EUTRA and NB-IoT are in Table VI.

APPENDIX B

PROOF OF LEMMAS AND THEOREMS

A. Proof of Theorem 1

Considering the separation of variables, i.e., $u(z, t) = Z(z) \cdot e^{j\omega t}$, and defining the phase velocity $c_v \triangleq \sqrt{\frac{c^D}{\rho}}$ of the vibration module along the z-axis, the wave equation $Z(z)$ is given as follows,

$$\begin{aligned} \omega^2 Z + \frac{c^D}{\rho} \frac{d^2 Z}{dz^2} &= 0, \\ \frac{d^2 Z}{dz^2} + \frac{\omega^2}{c_v^2} Z &= 0, \end{aligned} \quad (32)$$

whose formal solution is

$$\begin{aligned} Z(z) &= A \sin(\beta z) + B \cos(\beta z), \\ \beta &= \frac{\omega}{c_v}. \end{aligned} \quad (33)$$

According to Maxwell equation $\nabla \cdot D = \rho_{free} = 0$, the electric displacement vector is a variable only related to time, which can be expressed as $D(z, t) = D(t) = D_0 e^{j\omega t}$. Substituting boundary condition $T|_{z=0} = T|_{z=L_T} = 0$ into the solution, then we can get that $A = e_{33} D_0 / (\epsilon^S c^D \beta)$ and $B = A(\cos(\beta L_T) - 1) / (\sin(\beta L_T))$. A complete solution can be given by

$$u(z, t) = \frac{e_{33} D_0}{\epsilon^S c^D \beta} \left[\frac{\cos(\beta(L_T - z)) - \cos(\beta L_T)}{\sin(\beta L_T)} \right] e^{j\omega t}. \quad (34)$$

The surface vibration at $z = L_T$ is given by

$$\begin{aligned} u(L_T, t) &= \frac{e_{33} D_0}{\epsilon^S c^D \beta} \left[\frac{1 - \cos(\beta L_T)}{\sin(\beta L_T)} \right] e^{j\omega t}, \\ &= \frac{e_{33} D_0}{\epsilon^S c^D \beta} \tan\left(\frac{\beta L_T}{2}\right) e^{j\omega t}. \end{aligned} \quad (35)$$

TABLE IV
REFERENCE SENSITIVITY POWER LEVELS IN EUTRA BASE STATIONS.

Base station types	Bandwidth [MHz]	Reference sensitivity power level [dBm]
Wide Area Base Station	5	-101.5
Local Area Base Station	5	-93.5
Home Base Station	5	-93.5
Medium Range a Base Station	5	-96.5
Note: The reference measurement channel is specified in Annex A1-3 in [33].		

TABLE V
REFERENCE SENSITIVITY POWER LEVELS IN NB-IoT BASE STATIONS.

Base station types	Bandwidth [kHz]	Reference sensitivity power level [dBm]
Wide Area Base Station	3.75	-133.3
Local Area Base Station	3.75	-125.3
Home Base Station	3.75	-125.3
Medium Range a Base Station	3.75	-128.3
Note: The reference measurement channel is specified in Annex A14-2 in [33].		

TABLE VI
REFERENCE SENSITIVITY POWER LEVEL AT NORMALIZED BANDWIDTH.

Base station types		Reference sensitivity power level [dBm]
E-UTRA	Wide Area Base Station	-133.7
	Local Area Base Station	-125.7
	Home Base Station	-125.7
	Medium Range a Base Station	-128.7
NB-IoT	Wide Area Base Station	-134.3
	Local Area Base Station	-126.3
	Home Base Station	-126.3
	Medium Range a Base Station	-129.3

Integrate the electric field E in the z direction to obtain the expression of the electric potential as follows

$$\begin{aligned}
V &= V_0 \cdot e^{j\omega t} \\
&= \int_0^{L_T} E(z, t) dz = \int_0^{L_T} \frac{1}{\epsilon^S} (D - eS) dz \\
&= \frac{DL_T}{\epsilon^S} - \frac{e_{33}}{\epsilon^S} (u(L_T, t) - u(0, t)) \\
&= \left\{ \frac{D_0 L_T}{\epsilon^S} - \frac{e_{33}}{\epsilon^S} [u(L_T, 0) - u(0, 0)] \right\} \cdot e^{j\omega t} \\
&= \left[\frac{D_0 L_T}{\epsilon^S} - \frac{2e_{33}^2 D_0}{(\epsilon^S)^2 c^D \beta} \tan\left(\frac{\beta L_T}{2}\right) \right] \cdot e^{j\omega t},
\end{aligned} \tag{36}$$

where k_t is electromechanical coupling coefficient, a parameter that characterizes the properties of piezoelectric films. It is easy to obtain the expression of D_0 as follows

$$D_0 = \frac{V_0}{\left[\frac{L_T}{\epsilon^S} - \frac{2k_t^2}{\epsilon^S \beta} \tan\left(\frac{\beta L_T}{2}\right) \right]}. \tag{37}$$

B. Proof of Theorem 2

Considering the separation of variables, i.e., $v(z, t) = V(z) \cdot e^{j\omega t}$, the wave equation $V(z)$ is given as follows,

$$c^D \frac{d^2 V}{dz^2} + j\omega\eta \frac{dV}{dz} = -\rho\omega^2 V, \tag{38}$$

$$\begin{aligned}
V(z) &= A \sin(\hat{\beta}z) + B \cos(\hat{\beta}z), \\
\hat{\beta} &= \sqrt{\frac{\rho\omega^2}{c^D + j\omega\eta}},
\end{aligned} \tag{39}$$

where $\hat{\beta} = \beta / \sqrt{1 + \frac{j\omega\eta}{c^D}} \approx \beta + j\alpha$; $\beta = \frac{\omega}{c_v}$, $\alpha = \frac{\eta\omega\beta}{2c^D}$ and $Q = \left(\frac{\eta\omega}{c^D}\right)^{-1}$. According to Eq. (35), the surface vibration at $z = L_T$ is given by

$$u(L_T, t) = \frac{e_{33} \cdot D_0}{\epsilon^S \cdot c^D \cdot \hat{\beta}} \tan\left(\frac{\hat{\beta} L_T}{2}\right) \cdot e^{j\omega t}. \tag{40}$$

Based on the series resonance condition, $\tan\left(\frac{\beta L_T}{2}\right) = \frac{\beta L_T/2}{k_t^2}$, we give the simplified solution as follows

$$\begin{aligned}
u(L_T, t) &= \frac{e \cdot D_0}{\epsilon^S \cdot c^D \cdot \hat{\beta}} \tan\left(\frac{\hat{\beta} L_T}{2}\right) \cdot e^{j\omega t} \\
&\approx -j \frac{4V_0 d_{33} Q}{\pi^2} \cdot e^{j\omega t}.
\end{aligned} \tag{41}$$

According to Eq. (37), the amplitude of electric displacement vector is approximated by

$$\begin{aligned} D_0 &= \frac{V_0 \epsilon^S / L_T}{\left[1 - k_t^2 \frac{\tan(\beta L_T / 2)}{\beta L_T / 2} \right]} \\ &\approx \frac{V_0 \epsilon^S / L_T}{1 - \frac{k_t^2}{k_t^2 + j \frac{\pi^2}{2Q}}} \\ &= \frac{V_0 \epsilon^S}{L_T} \left(1 - j \frac{2Q k_t^2}{\pi^2} \right). \end{aligned} \quad (42)$$

C. Proof of Theorem 3

Here, the mechanical vibration part is equivalent to the ordinary harmonic oscillator, and its Hamilton value in the phase space and Fock space is as follows,

$$H_p = \frac{p^2}{2m} + \frac{1}{2} m \omega_M^2 x^2 = \hbar \omega_M b^\dagger b, \quad (43)$$

where p and x are the momentum and coordinates of the piezoelectric oscillator, respectively; m is the effective mass of the piezoelectric oscillator; and ω_M is its resonance frequency. Note that the annihilation operator in Fock space is $b = \sqrt{\frac{m \omega_M}{2 \hbar}} \left(x + \frac{i p}{m \omega_M} \right)$.

Hamiltonian of the resonant circuit is given by

$$H_e = \frac{q^2}{2C(x)} + \frac{\phi^2}{2L} = \hbar \omega_{LC} a^\dagger a, \quad (44)$$

where ϕ and q are flux on inductor and charge on capacitor, respectively; and $\omega_{LC} = \frac{1}{\sqrt{LC}}$ represents the resonance frequency of LC circuit. Similarly, the annihilation operator in Fock space is $a = \sqrt{\frac{1}{2 \hbar \omega_{LC} C(x)}} \left(q + \frac{i \phi}{\omega_{LC} L} \right)$.

Moreover, the coupling term is given by

$$\begin{aligned} H_{pe} &= \hbar g (b^\dagger + b) (a + a^\dagger), \\ &= \hbar g A_0 B_0 [b^\dagger a + b^\dagger a^\dagger + b a + b a^\dagger], \\ &= 4 \hbar g A_0 B_0 x q, \end{aligned} \quad (45)$$

where $A_0 = \sqrt{\frac{1}{2 \hbar \omega_{LC} C(x)}}$ and $B_0 = \sqrt{\frac{m \omega_M}{2 \hbar}}$, respectively.

Hamiltonian in classical form is given by

$$\begin{aligned} H &= \frac{p^2}{2m} + \frac{m \omega_M^2 x^2}{2} + \frac{\phi^2}{2L} + \frac{q^2}{2C(x)} + \\ &2g \sqrt{\frac{m \omega_M}{C(x) \omega_{LC}}} x q - q V. \end{aligned} \quad (46)$$

Under resonance condition, $\omega_M = \omega_{LC} = \omega_r$. The canonical equations are given as follows,

$$\begin{aligned} \frac{\partial H}{\partial p} &= \dot{x}, \\ \frac{\partial H}{\partial x} &= -\dot{p}, \end{aligned} \quad (47)$$

and

$$\begin{aligned} \dot{p} &= -\frac{\partial H}{\partial x} \\ &= -m \omega_r^2 x - \frac{q^2}{2} \frac{\partial}{\partial x} \left(\frac{1}{C(x)} \right) - 2g \sqrt{m} \frac{\partial}{\partial x} \left(\frac{x}{\sqrt{C(x)}} \right) q, \end{aligned} \quad (48)$$

$$\begin{aligned} \dot{\phi} &= -\frac{\partial H}{\partial q}, \\ &= -\frac{q}{C(x)} - 2g \sqrt{m} \frac{x}{\sqrt{C(x)}} + V. \end{aligned}$$

Assuming a real system with random disturbance, the Langevin Equations are given by

$$\begin{aligned} \dot{x} &= \frac{p}{m}, \\ \dot{p} &= -m \omega_r^2 x - \frac{q^2}{2} \frac{\partial}{\partial x} \left(\frac{1}{C(x)} \right) - 2g \sqrt{m} \frac{\partial}{\partial x} \left(\frac{x}{\sqrt{C(x)}} \right) q \\ &\quad - \Gamma_m p - F, \\ \dot{\phi} &= \frac{\phi}{L}, \\ \dot{q} &= -\frac{q}{C(x)} - 2g \sqrt{m} \frac{x}{\sqrt{C(x)}} - \Gamma_{LC} \phi + V. \end{aligned} \quad (49)$$

Assume that the equivalent force of the thermal motion δF_{th} is the only force. We select the first order perturbation around the equilibrium point $\bar{x} = \bar{p} = \bar{q} = \bar{\phi} = 0$. The first order perturbation equations are as follows,

$$\begin{aligned} \delta \dot{x} &= \frac{\delta p}{m}, \\ \delta \dot{p} &= -m \omega_r^2 \delta x - \frac{\bar{q}^2}{2} \frac{\partial^2}{\partial x^2} \left(\frac{1}{C(x)} \right)_{x=\bar{x}} \delta x \\ &\quad - \bar{q} \frac{\partial}{\partial x} \left(\frac{1}{C(x)} \right)_{x=\bar{x}} \delta q - 2 \bar{q} g \sqrt{m} \frac{\partial^2}{\partial x^2} \left(\frac{x}{\sqrt{C(x)}} \right)_{x=\bar{x}} \delta x \\ &\quad - 2g \sqrt{m} \frac{\partial}{\partial x} \left(\frac{x}{\sqrt{C(x)}} \right)_{x=\bar{x}} \delta q - \Gamma_m \delta p - \delta F_{th}, \\ \delta \dot{q} &= \frac{\delta \phi}{L}, \\ \delta \dot{\phi} &= -\frac{\delta q}{C(\bar{x})} - \bar{q} \frac{\partial}{\partial x} \left(\frac{1}{C(x)} \right)_{x=\bar{x}} \delta x \\ &\quad - 2g \sqrt{m} \frac{\partial}{\partial x} \left(\frac{x}{\sqrt{C(x)}} \right)_{x=\bar{x}} \delta x - \Gamma_{LC} \delta \phi + \delta V. \end{aligned} \quad (50)$$

Transforming the analysis from time domain to frequency domain, we can get the equations as follows,

$$\begin{aligned} -i \Omega \delta x(\Omega) &= \frac{\delta p(\Omega)}{m}, \\ -i \Omega \delta p(\Omega) &= -m \omega_r^2 \delta x(\Omega) - 2g \sqrt{\frac{m}{C(\bar{x})}} \delta q(\Omega) \\ &\quad - \Gamma_m \delta p(\Omega) - \delta F_{th}(\Omega), \\ -i \Omega \delta q(\Omega) &= \frac{\delta \phi(\Omega)}{L}, \\ -i \Omega \delta \phi(\Omega) &= -\frac{\delta q(\Omega)}{C(\bar{x})} - 2g \sqrt{\frac{m}{C(\bar{x})}} \delta x(\Omega) \\ &\quad - \Gamma_{LC} \delta \phi(\Omega) + \delta V(\Omega). \end{aligned} \quad (51)$$

Redefine the coupling coefficient $G = 2g\sqrt{\frac{m}{C(\bar{x})}} = 2g\sqrt{\frac{mL_F}{\epsilon^S A}}$, the equations in frequency domain are given as follows,

$$\begin{aligned} -i\Omega\delta x(\Omega) &= \frac{\delta p(\Omega)}{m}, \\ -i\Omega\delta p(\Omega) &= -m\omega_r^2\delta x(\Omega) - \Gamma_m\delta p(\Omega) - G\delta q(\Omega) - \delta F_{th}(\Omega), \\ -i\Omega\delta q(\Omega) &= \frac{\delta\phi(\Omega)}{L}, \\ -i\Omega\delta\phi(\Omega) &= -\frac{\delta q(\Omega)}{C(\bar{x})} - \Gamma_{LC}\delta\phi(\Omega) - G\delta x(\Omega) + \delta V(\Omega). \end{aligned} \quad (52)$$

According to the above equation, the response of the system to force or voltage signal excitation can be calculated. For piezoelectric oscillator and LC circuit, two parameters are defined as follows,

$$\begin{aligned} \chi_m(\Omega) &= \frac{1}{m(\Omega_m^2 - \Omega^2 - i\Omega\Gamma_m)}, \\ \chi_{LC}(\Omega) &= \frac{1}{L(\Omega_{LC}^2 - \Omega^2 - i\Omega\Gamma_{LC})}. \end{aligned} \quad (53)$$

Again, the equations in frequency domain can be written as follows,

$$\begin{aligned} \chi_m(\Omega)(-\delta F_{th}(\Omega) + G\chi_{LC}(\Omega)\delta V(\Omega)) \\ = \left(1 - G^2\chi_m(\Omega)\chi_{LC}(\Omega)\right)\delta x(\Omega), \\ \delta x(\Omega) = \left(\chi_m(\Omega)^{-1} - G^2\chi_{LC}(\Omega)\right)^{-1} \\ (-\delta F_{th}(\Omega) + G\chi_{LC}(\Omega)\delta V(\Omega)). \end{aligned} \quad (54)$$

Defining $\chi_m^{eff}(\Omega) \triangleq \left(\chi_m(\Omega)^{-1} - G^2\chi_{LC}(\Omega)\right)^{-1}$, the transfer function of the system in frequency domain is given by

$$\begin{aligned} \delta x(\Omega) &= \chi_m^{eff}(-\delta F_{th}(\Omega) + G\chi_{LC}(\Omega)\delta V(\Omega)), \\ \delta\varphi(\Omega) &= 2k\chi_m^{eff}(-\delta F_{th}(\Omega) + G\chi_{LC}(\Omega)\delta V(\Omega)) \\ &\quad + \delta\varphi_{im}(\Omega), \end{aligned} \quad (55)$$

where $\delta\varphi = 2k\delta x$ ($k = 2\pi/\lambda$) represents the phase variation to δx .

Moreover, considering the light force of the optical cavity in a real system, the expression of $\chi_m(\omega)$ is modified as follows,

$$\begin{aligned} \chi_{m,eff}^{-1}(\omega) &= \chi_m^{-1}(\omega) + \Sigma(\omega), \\ \Sigma(\omega) &= 2m_{eff}\Omega_m g^2 \left\{ \frac{1}{(\Delta + \omega) + i\kappa/2} + \frac{1}{(\Delta - \omega) - i\kappa/2} \right\}, \end{aligned} \quad (56)$$

where Δ and κ represent the laser detuning to the optical cavity and attenuation coefficient, respectively.

Then, we introduce two parameters $\delta\Omega_m$ and Γ_{opt} as follows,

$$\begin{aligned} \delta\Omega_m(\omega) &= g^2 \frac{\Omega_m}{\omega} \left[\frac{\Delta + \omega}{(\Delta + \omega)^2 + \kappa^2/4} + \frac{\Delta - \omega}{(\Delta - \omega)^2 + \kappa^2/4} \right], \\ \Gamma_{opt}(\omega) &= g^2 \frac{\Omega_m}{\omega} \left[\frac{\kappa}{(\Delta + \omega)^2 + \kappa^2/4} - \frac{\kappa}{(\Delta - \omega)^2 + \kappa^2/4} \right], \end{aligned} \quad (57)$$

where $\delta\Omega_m$ and Γ_{opt} represent frequency shift and damping coefficient variation caused by light incident, respectively. Substituting them into Eq. (56), we have

$$\begin{aligned} \Sigma(\omega) &\equiv m_{eff}\omega [2\delta\Omega_m(\omega) - i\Gamma_{opt}(\omega)], \\ \chi_{m,eff}^{-1}(\omega) &= m_{eff} [\Omega_m^2 + 2\omega\delta\Omega_m(\omega) - \omega^2] \\ &\quad - i\omega m_{eff} [\Gamma_m + \Gamma_{opt}(\omega)]. \end{aligned} \quad (58)$$

Under different cavity attenuation sizes κ , the form of frequency detuning is not exactly the same. The frequency drift introduced by the optical field is called the optical spring effect, which disappears under certain detuning conditions. Moreover, the radiation pressure in the cavity will produce equivalent cooling and amplification effects on the motion of the end mirror (in our system, it is represented by piezoelectric film).

D. Proof of Theorem 4

In our system, the response of piezoelectric film to RF signals can be approximated as a damped harmonic oscillator model. The vibration equation is given by

$$m_{eff} \frac{dx^2(t)}{dt^2} + m_{eff}\Gamma_m \frac{dx(t)}{dt} + m_{eff}\Omega_m^2 x(t) = \eta_{ex}(t). \quad (59)$$

In the equilibrium, the environment exerts a disturbing force η_{ex} on the damped harmonic oscillator. Defining $\eta(t) \triangleq \eta_{ex}(t)/m_{eff}$, the vibration equation is simplified as follows,

$$\frac{dx^2(t)}{dt^2} + \Gamma_m \frac{dx(t)}{dt} + \Omega_m^2 x(t) = \eta(t). \quad (60)$$

According to the white noise hypothesis, $\eta(t)$ satisfies the following equations,

$$\langle \eta(t) \rangle = 0, \quad \langle \eta(t)\eta(\tau) \rangle = 2\alpha\delta(t - \tau). \quad (61)$$

A solution is given by

$$\begin{aligned} x(t) &= a_{10}e^{\mu_1 t} + a_{20}e^{\mu_2 t} \\ &\quad + \frac{1}{\mu_1 - \mu_2} \int_0^t [e^{\mu_1(t-t')} - e^{\mu_2(t-t')}] \eta(t') dt', \end{aligned} \quad (62)$$

where μ_1 and μ_2 are the two solutions to $\mu^2 + \Gamma_m\mu + \Omega_m^2 = 0$, respectively. Under weak stationary condition, the correlation function of simple harmonic noise is given by [34]

$$\langle x(t)x(\tau) \rangle = \frac{\alpha}{\mu_1^2 - \mu_2^2} \left[\frac{1}{\mu_1} e^{\mu_1|t-\tau|} - \frac{1}{\mu_2} e^{\mu_2|t-\tau|} \right]. \quad (63)$$

Fourier transform is applied to the above equation to obtain the simple harmonic noise power spectrum as follows,

$$S(\omega) = 2\alpha_{ex} |\chi_m(\omega)|^2, \quad (64)$$

where $\alpha_{ex} = \alpha m_{eff}^2$ represents the noise strength.

REFERENCES

- [1] T. Bagci, A. Simonsen, S. Schmid, L. G. Villanueva, E. Zeuthen, J. Appel, J. M. Taylor, A. Sørensen, K. Usami, A. Schliesser, *et al.*, “Optical detection of radio waves through a nanomechanical transducer,” *Nature*, vol. 507, no. 7490, pp. 81–85, 2014.
- [2] C. Regal and K. Lehnert, “From cavity electromechanics to cavity optomechanics,” in *Journal of Physics: Conference Series*, vol. 264, no. 1. IOP Publishing, 2011, p. 012025.
- [3] A. H. Safavi-Naeini and O. Painter, “Proposal for an optomechanical traveling wave phonon–photon translator,” *New Journal of Physics*, vol. 13, no. 1, p. 013017, 2011.
- [4] J. M. Taylor, A. S. Sørensen, C. M. Marcus, and E. S. Polzik, “Laser cooling and optical detection of excitations in a l c electrical circuit,” *Physical Review Letters*, vol. 107, no. 27, p. 273601, 2011.
- [5] S. Barzanjeh, M. Abdi, G. J. Milburn, P. Tombesi, and D. Vitali, “Reversible optical-to-microwave quantum interface,” *Physical Review Letters*, vol. 109, no. 13, p. 130503, 2012.
- [6] Y.-D. Wang and A. A. Clerk, “Using interference for high fidelity quantum state transfer in optomechanics,” *Physical Review Letters*, vol. 108, no. 15, p. 153603, 2012.
- [7] L. Tian, “Adiabatic state conversion and pulse transmission in optomechanical systems,” *Physical Review Letters*, vol. 108, no. 15, p. 153604, 2012.
- [8] —, “Optoelectromechanical transducer: Reversible conversion between microwave and optical photons,” *Annalen der Physik*, vol. 527, no. 1-2, pp. 1–14, 2015.
- [9] L. Midolo, A. Schliesser, and A. Fiore, “Nano-opto-electro-mechanical systems,” *Nature Nanotechnology*, vol. 13, no. 1, pp. 11–18, 2018.
- [10] K. Liu, C. R. Ye, S. Khan, and V. J. Sorger, “Review and perspective on ultrafast wavelength-size electro-optic modulators,” *Laser & Photonics Reviews*, vol. 9, no. 2, pp. 172–194, 2015.
- [11] T. J. Kippenberg and K. J. Vahala, “Cavity optomechanics: back-action at the mesoscale,” *Science*, vol. 321, no. 5893, pp. 1172–1176, 2008.
- [12] M. Aspelmeyer, T. J. Kippenberg, and F. Marquardt, “Cavity optomechanics,” *Reviews of Modern Physics*, vol. 86, no. 4, p. 1391, 2014.
- [13] A. D. O’Connell, M. Hofheinz, M. Ansmann, R. C. Bialczak, M. Lenander, E. Lucero, M. Neeley, D. Sank, H. Wang, M. Weides, *et al.*, “Quantum ground state and single-phonon control of a mechanical resonator,” *Nature*, vol. 464, no. 7289, pp. 697–703, 2010.
- [14] J. D. Teufel, D. Li, M. Allman, K. Cicak, A. Sirois, J. Whittaker, and R. Simmonds, “Circuit cavity electromechanics in the strong-coupling regime,” *Nature*, vol. 471, no. 7337, pp. 204–208, 2011.
- [15] T. Faust, P. Krenn, S. Manus, J. P. Kotthaus, and E. M. Weig, “Microwave cavity-enhanced transduction for plug and play nanomechanics at room temperature,” *Nature Communications*, vol. 3, no. 1, pp. 1–6, 2012.
- [16] S. Gröblacher, K. Hammerer, M. R. Vanner, and M. Aspelmeyer, “Observation of strong coupling between a micromechanical resonator and an optical cavity field,” *Nature*, vol. 460, no. 7256, pp. 724–727, 2009.
- [17] E. Verhagen, S. Deléglise, S. Weis, A. Schliesser, and T. J. Kippenberg, “Quantum-coherent coupling of a mechanical oscillator to an optical cavity mode,” *Nature*, vol. 482, no. 7383, pp. 63–67, 2012.
- [18] C. Zuo, J. Van der Spiegel, and G. Piazza, “1.05-GHz CMOS oscillator based on lateral-field-excited piezoelectric AlN contour-mode MEMS resonators,” *IEEE Transactions on Ultrasonics, Ferroelectrics, and Frequency control*, vol. 57, no. 1, pp. 82–87, 2009.
- [19] C. Zuo, C. H. Yun, P. J. Stephanou, S.-J. Park, C.-S. T. Lo, R. Mikulka, J.-H. J. Lan, M. F. Velez, R. V. Shenoy, J. Kim, *et al.*, “Cross-sectional dilation mode resonator with very high electromechanical coupling up to 10% using AlN,” in *2012 IEEE International Frequency Control Symposium Proceedings*. IEEE, 2012, pp. 1–4.
- [20] C. Zuo, C. He, W. Cheng, and Z. Wang, “Hybrid Filter Design for 5G using IPD and Acoustic Technologies,” in *2019 IEEE International Ultrasonics Symposium (IUS)*. IEEE, 2019, pp. 269–272.
- [21] K. Tonisch, V. Cimalla, C. Foerster, H. Romanus, O. Ambacher, and D. Dontsov, “Piezoelectric properties of polycrystalline AlN thin films for MEMS application,” *Sensors and Actuators A: Physical*, vol. 132, no. 2, pp. 658–663, 2006.
- [22] C. Zuo, N. Sinha, and G. Piazza, “Very high frequency channel-select MEMS filters based on self-coupled piezoelectric AlN contour-mode resonators,” *Sensors and Actuators A: Physical*, vol. 160, no. 1-2, pp. 132–140, 2010.
- [23] C. Zuo, N. Sinha, J. Van der Spiegel, and G. Piazza, “Multifrequency pierce oscillators based on piezoelectric AlN contour-mode MEMS technology,” *Journal of Microelectromechanical Systems*, vol. 19, no. 3, pp. 570–580, 2010.
- [24] A. Abramovici, W. E. Althouse, R. W. P. Drever, Y. Gursel, S. Kawamura, F. J. Raab, D. Shoemaker, L. Sievers, R. E. Spero, and K. S. Thorne, “LIGO: The Laser Interferometer Gravitational-Wave Observatory,” *Science*, vol. 256, no. 5055, pp. 325–333.
- [25] A. Freise and K. Strain, “Interferometer techniques for gravitational-wave detection,” *Living Reviews in Relativity*, vol. 13, no. 1, p. 1, 2010.
- [26] A. Arnau *et al.*, *Piezoelectric transducers and applications*. Springer, 2004, vol. 2004.
- [27] J. Rosenbaum, *Bulk acoustic wave theory and devices*. Artech House on Demand, 1988.
- [28] C.-L. Zou, X. Han, L. Jiang, and H. X. Tang, “Cavity piezomechanical strong coupling and frequency conversion on an aluminum nitride chip,” *Physical Review A*, vol. 94, no. 1, p. 013812, 2016.
- [29] “Comsol multiphysics® v. 5.4,” *cn.comsol.com. COMSOL AB, Stockholm, Sweden*.
- [30] A. Freise, D. Brown, and C. Bond, “Finesse, frequency domain interferometer simulation software,” *arXiv preprint arXiv:1306.2973*, 2013.
- [31] N. Wadefalk, R. Gawande, and S. Weinreb, “Very low noise amplifiers at 300 K for 0.7 to 1.4 GHz,” in *Proc. National Radio Science Meeting (URSI)*, 2005.
- [32] J.-B. Wang, Q.-S. Hu, J. Wang, M. Chen, and J.-Y. Wang, “Tight bounds on channel capacity for dimmable visible light communications,” *IEEE Journal of Lightwave Technology*, vol. 31, no. 23, pp. 3771–3779, 2013.
- [33] T. ETSI, “136 104 v16. 4.0, lte; evolved universal terrestrial radio access (e-utra); base station (bs) radio transmission and reception (3gpp ts 36.104 version 16.4. 0 release 16), december 2019,” *FRANCE: ETSI (3GPP)*, pp. 36 104–20, 2019.
- [34] J. Bao, *Random Simulation Method of Classical and Quantum Dissipation System*. Beijing Science Press, 2009.